Robust Short-Lag Spatial Coherence Imaging of Breast Ultrasound Data: Initial Clinical Results

Alycen Wiacek, *Student Member, IEEE,* Ole Marius Hoel Rindal, *Student Member, IEEE,* Eniola Falomo, Kelly Myers, Kelly Fabrega-Foster, Susan Harvey, and Muyinatu A. Lediju Bell, *Member, IEEE*

***Abstract*— Ultrasound is frequently used in conjunction with mammography in order to detect breast cancer as early as possible. However, due largely to the heterogeneity of breast tissue, ultrasound images are plagued with clutter that obstructs important diagnostic features. Short-lag spatial coherence (SLSC) imaging has proven to be effective at clutter reduction in noisy ultrasound images. *M*-Weighted SLSC and Robust-SLSC (R-SLSC) imaging were recently introduced to further improve image quality at higher lag values, while R-SLSC imaging has the added benefit of enabling the adjustment of tissue texture to produce a tissue signal-to-noise ratio (SNR) that is quantitatively similar to B-mode speckle SNR. This paper investigates the initial application of SLSC, *M*-Weighted SLSC, and R-SLSC imaging to nine targets in the female breast [two simple cysts, one complicated cyst, two fibroadenomas, one hematoma, one complex cystic and solid mass, one invasive ductal carcinoma (IDC), and one ductal carcinoma *in situ* (DCIS)]. As expected, R-SLSC beamforming improves cyst and hematoma contrast by up to 6.35 and 1.55 dB, respectively, when compared to the original B-mode image, and similar improvements are achieved with SLSC and *M*-Weighted SLSC imaging. However, an interesting finding from this initial investigation is that the solid masses (i.e., fibroadenoma, complex cystic and solid mass, IDC, and DCIS), which appear as hypoechoic in the B-mode image, have similarly high coherence to that of surrounding tissue in coherence-based images. This work holds promise for using SLSC, *M*-Weighted SLSC, and/or R-SLSC imaging to distinguish between fluid-filled and solid hypoechoic breast masses.**

***Index Terms*— Breast ultrasound, coherence-based beamforming, compressed sensing, ultrasonic imaging.**

I. Introduction

BREAST cancer is the most common cancer among women, and the second leading cause of cancer death [1]. Over 250 000 women will be diagnosed with breast cancer in the United States in 2018 and more than 40 000 women will die from the disease [1]. It is well documented that early detection results in dramatically improved morbidity and mortality [2]. Currently, mammography is the screening modality of choice, and it is considered one of the most important imaging methods to reduce the likelihood of death from breast cancer [3]. However, mammographic sensitivity (i.e., the ability of a mammogram to detect cancer) is significantly lower in patients with dense breast tissue [4]. When breast tissue is dense, the surrounding parenchyma can often obscure diagnostic features in the mammogram, necessitating a supplement, such as ultrasound, in order to improve detection. Ultrasound is cost efficient, portable, does not use ionizing radiation, and is generally painless, but low specificity and other challenges have led to its slow uptake as a screening tool.

Challenges with ultrasound imaging include the presence of various noise artifacts, including clutter, which arises from multipath acoustic interactions between tissue layers, phase aberration, and off-axis scattering [5], [6]. These artifacts obscure important diagnostic features and complicate clinical decisions [5]. Due to the heterogeneity of breast tissue (which is a major characteristic of dense breast tissue), breast ultrasound images tend to be particularly cluttered, causing incoherent noise within hypoechoic or anechoic regions [7], [8]. Therefore, recent advances in ultrasound beamforming technology to reduce clutter and improve contrast and resolution are well suited for breast applications.

One technique known to reduce clutter is harmonic imaging, which receives the higher harmonics of the reflected ultrasound waves instead of reflections at the fundamental frequency. This technique improves lateral resolution (due to the increased receive frequency), at the expense of axial resolution (due to the smaller receive bandwidth) [9]. Given this tradeoff between axial and lateral resolutions, van Wijk and Thijssen [9] found that lesion detection in a tissue mimicking phantom is not significantly improved with harmonic imaging. Another option for clutter reduction in breast imaging is coherence-based imaging [10]. For example, Li and Li [11] proposed the use of a generalized coherence factor (GCF) that suppresses clutter-causing sidelobes by adaptively weighting B-mode images with the GCF.

Another clutter reduction technique is short-lag spatial coherence (SLSC) imaging, which directly displays the spatial coherence between closely spaced elements in order to reduce clutter in ultrasound images [12]. The first *in vivo*

Manuscript received August 3, 2018; accepted November 20, 2018. Date of publication November 27, 2018; date of current version March 14, 2019. This work was supported in part by the NIH under Grant R00-EB018994. *(Corresponding author: Alycen Wiacek.)*

A. Wiacek is with the Department of Electrical and Computer Engineering, Johns Hopkins University, Baltimore, MD 21218 USA (e-mail: awiacek1@jhu.edu).

O. M. H. Rindal is with the Department of Informatics, University of Oslo, 0373 Oslo, Norway.

E. Falomo, K. Myers, K. Fabrega-Foster, and S. Harvey are with the Department of Radiology and Radiological Science, Johns Hopkins Medicine, Baltimore, MD 21287 USA.

M. A. L. Bell is with the Department of Electrical and Computer Engineering, Johns Hopkins University, Baltimore, MD 21218 USA, and also with the Department of Biomedical Engineering, Johns Hopkins University, Baltimore, MD 21218 USA.

Digital Object Identifier 10.1109/TUFFC.2018.2883427

demonstration of SLSC imaging showed reduced clutter in a human thyroid [12]. SLSC imaging has since been applied to a variety of clinical ultrasound data [13]–[16]. Although the resolution and contrast improvements in these cases depend on multiple parameters [17], SLSC imaging has generally shown improvements over standard B-mode imaging with regard to the visualization of endocardial borders [13], vessels in the liver [15], and fetal structures [14], [16]. SLSC imaging has also demonstrated improved capabilities for lesion detectability in the presence of noise and clutter [17], [18]. SLSC beamforming relies on the principle that the best tradeoff among contrast, tissue signal-to-noise ratio (SNR), contrast-to-noise ratio (CNR), and resolution occurs in the short-lag region. Including additional lags adds more high-frequency information, and thereby improves the lateral resolution of SLSC images [17]. However, the coherence estimated at these additional, higher lags has high variance, which causes a degradation in image contrast.

Nair *et al*. [19] presented Robust-SLSC (R-SLSC) and M-Weighted SLSC imaging to improve the tradeoff among contrast, resolution, and SNR at higher short-lag values by applying robust principal component analysis (RPCA) to vectorized lag images. The result is a denoised data matrix that is then weighted to place greater emphasis on the short-lag images. The latter step can also be applied without RPCA, resulting in M-Weighted SLSC images. Tested with simulation, phantom, and *in vivo* liver data [19], R-SLSC and M-Weighted SLSC imaging demonstrate the ability to smooth tissue texture and enhance target visibility at higher lag values. These improvements have implications for improving lesion detectability in heterogeneous breast tissue.

In this paper, we present our initial results of SLSC, M-Weighted SLSC, and R-SLSC imaging applied to clinical breast ultrasound data. We additionally address the clinical tradeoff of these methods and discuss outstanding challenges with deploying these methods in breast clinics.

II. Background

A. Short-Lag Spatial Coherence Imaging

SLSC imaging relies on measurements of the spatial coherence of backscattered echoes received across the transducer aperture [20], [21]. While standard B-mode images display the echogenicity of tissue, SLSC imaging does not use this brightness information, instead displaying differences in tissue based on the similarity of the received acoustic waveforms [14].

Based on this principle, SLSC imaging can be described by two main equations. Equation (1) defines spatial coherence $\hat{R}$ as a measure of the similarity of backscattered echoes. It is calculated by normalizing the spatial covariance across the receive aperture by the variance of each signal [22]

$$\hat{R}(m) = \frac{1}{N-m}\sum_{i=1}^{N-m}\frac{\sum_{n=n_1}^{n_2} s_i(n)s_{i+m}(n)}{\sqrt{\sum_{n=n_1}^{n_2} s_i^2(n)\sum_{n=n_1}^{n_2} s_{i+m}^2(n)}} \quad (1)$$

where m is the lag (i.e., the number of elements between two points in the aperture), N is the number of elements in the transducer, and $s_i(n)$ is a time-delayed, zero-mean signal received at element i from depth n.

Equation (2) states that the spatial coherence in the short-lag region, R_{sl}, is equal to the integral over the first M lags

$$R_{sl} = \int_1^M \hat{R}(m)dm \approx \sum_{m=1}^{M}\hat{R}(m). \quad (2)$$

Equations (1) and (2) are used in succession when creating an SLSC image, which is formed pixel-wise by computing each equation at a depth n using a correlation kernel of size $k = n_2 - n_1$ [17], where k is typically taken to be one wavelength, centered on depth n. To create the final SLSC image, this process is repeated for each lateral and axial position.

B. Robust Short-Lag Spatial Coherence Imaging

Nair *et al*. [19] hypothesized that the images generated at different lags could be considered noisy versions of the true spatial coherence, particularly at higher lag values. Two new coherence-based beamforming approaches were implemented based on this hypothesis. Both approaches begin by vectorizing the lag images (i.e., the coherence images generated at each lag value up to lag value M) and stacking them horizontally.

The first approach employs RPCA to denoise this data matrix [23]. After some simplifications detailed in [19], the denoising process can be implemented with a minimization problem that can be solved using the augmented Lagrangian multiplier (ALM) method [24] to implement RPCA

$$L(A,E,Y,\mu) = ||A||_* + \lambda||E||_1 + \langle Y, D-A-E\rangle + \frac{\mu}{2}||D-A-E||_F^2 \quad (3)$$

where D is a noisy observation matrix (containing the stacked lag images) approximated by A, which is the low-rank ground truth matrix. E is a sparse error matrix, Y is a matrix of Lagrange multipliers, λ is the sparsity penalty parameter that can be varied to smooth tissue texture (note that this parameter is a multiplier of $(1/\sqrt{\text{size}(D,1)})$), μ is a positive scalar representing the reconstruction error ($\mu = (1.25/||D||_2)$ as recommended in [24]), $||\cdot||_1$ is the L_1 norm, $||\cdot||_F$ is the Frobenius norm, and $||\cdot||_*$ is the nuclear norm.

Following the denoising process, the denoised coherence matrix A is then weighted by a linearly decreasing weighting scheme as a function of M where the lag 1 image is assigned a weight of 1, and the lag M image is assigned a weight of $\frac{1}{M}$. This linear M-Weighting places more emphasis on the shorter lags while still including the higher resolution information from higher lags [19]. Finally, the vectorization is reversed to form the final R-SLSC image.

The second approach follows a similar rationale but does not include the RPCA step. Instead, after the lag images are vectorized and stacked, they are linearly M-Weighted (as described above), the vectorization is reversed, and the final M-Weighted SLSC image is formed.

Throughout this study, we used the MATLAB inexact ALM solver [24] hosted at [25] to perform RPCA.

TABLE I
IMAGE ACQUISITION DETAILS

Mass	Transducer	Center Frequency	Focus	Location
Cyst #1	L8-17	12.5 MHz	2 cm	2 o'clock radial, 6 cm from nipple
Cyst #2	L8-17	12.5 MHz	1 cm	6 o'clock anti-radial, 3 cm from nipple
Complicated Cyst	L8-17	12.5 MHz	0.7 cm	5 o'clock anti-radial, 2 cm from nipple
Hematoma	L8-17	12.5 MHz	2 cm	anti-radial
Fibroadenoma #1	L3-8	8 MHz	2 cm	8 o'clock radial, 2cm from nipple
Fibroadenoma #2	L8-17	12.5 MHz	1.2 cm	1 o'clock anti-radial, 5cm from nipple
Complex Cystic and Solid Mass	L8-17	12.5 MHz	1 cm	2 o'clock anti-radial, 12cm from nipple
IDC	L8-17	12.5 MHz	0.7 cm	9 o'clock radial, 3cm from nipple
DCIS	L8-17	12.5 MHz	1.2 cm	10 o'clock radial, 9cm from nipple

III. METHODS

A. Image Acquisition

Patients identified as having asymmetries from their routine mammograms volunteered to participate in this study. Informed consent was received, and our protocol was approved by the Johns Hopkins Medicine Institutional Review Board (protocol number IRB00127110).

The data from eight patients were selected based on findings in their clinical ultrasound images. The clinical diagnostic information was used to confirm and validate findings. Each patient had at least one of seven targets in their breast tissue: 1) simple cyst; 2) complicated cyst; 3) hematoma; 4) fibroadenoma; 5) complex cystic and solid mass; 6) invasive ductal carcinoma (IDC); and 7) ductal carcinoma *in situ* (DCIS). These seven targets were included in this study to compare B-mode, SLSC, M-Weighted SLSC, and R-SLSC breast images.

All data were acquired using the Alpinion Research Ultrasound Scanner (Alpinion, Seoul, South Korea). Raw channel data were saved for postprocedure processing. Each mass was insonified using a linear array ultrasound transducer with the parameters shown in Table I. Each transducer possessed 128 elements, with only 64 allowed to receive simultaneously, and used focused transmissions with 256 receive scan lines and a sampling frequency of 40 MHz. The focus was held constant at 2 cm for our first two patients (three masses), then varied to be consistent with the location of the mass for our remaining six patients (six masses).

B. Image Quality Metrics

In order to compare each imaging technique, the contrast, CNR, and tissue SNR were calculated for each data set as follows:

$$\text{Contrast} = 20\log_{10}\left(\frac{S_i}{S_o}\right) \tag{4}$$

$$\text{CNR} = \frac{|S_i - S_o|}{\sqrt{\sigma_i^2 + \sigma_o^2}} \tag{5}$$

$$\text{SNR} = \frac{S_o}{\sigma_o} \tag{6}$$

where S_i and σ_i are the mean and standard deviation, respectively, of beamformed signals prior to log compression within a region of interest (ROI) inside the target, and S_o and σ_o are similarly the mean and standard deviation, respectively, of signals within an ROI outside of the target, taken at approximately the same depth.

The ROIs for contrast and CNR calculations were chosen to be at the same depth and approximately the same area (in pixels). For the masses where the outside ROI was small, the ROI used for SNR calculations was chosen to be a larger region best representative of general tissue texture. The ROIs are not shown in the main text of this paper to facilitate the comparison between matched images, and they are instead included in the Appendix. Identical ROIs were used for each group of B-mode, SLSC, M-Weighted SLSC, and R-SLSC images, and each image grouping was generated using the same channel data. Each image group is also displayed with the same dynamic range to facilitate qualitative comparisons within each group. All signal processing and data analysis were performed with MATLAB software (MathWorks Inc., Natick, MA, USA).

C. Parameter Selection

1) Lag and Sparsity Parameters: The short-lag value M in SLSC images was chosen based on the selection methods from previous reports (i.e., lowest short-lag value with the best contrast [13]). The short-lag value for M-Weighted SLSC images was based on the R-SLSC parameter selection process; thus, the same short-lag value was used for both M-Weighted and R-SLSC images. In R-SLSC images, the sparsity parameter λ was varied along with the short-lag value M in order to determine the effect on image quality. Because speckle is often considered an important diagnostic property of ultrasound images, we selected M values and λ values to closely match the B-mode speckle SNR in the following two-step process.

Step 1) Simultaneously evaluate R-SLSC tissue SNR as functions of M and λ to select the combination of M and λ values that best match B-mode speckle SNR.

Step 2) Only if SNR values are similar for multiple possible λ values, examine the contrast measurements and select the combination of M and λ with the best contrast (i.e., improved by more than 0.1 dB, so as to not favor larger λ values with only minor improvements in contrast).

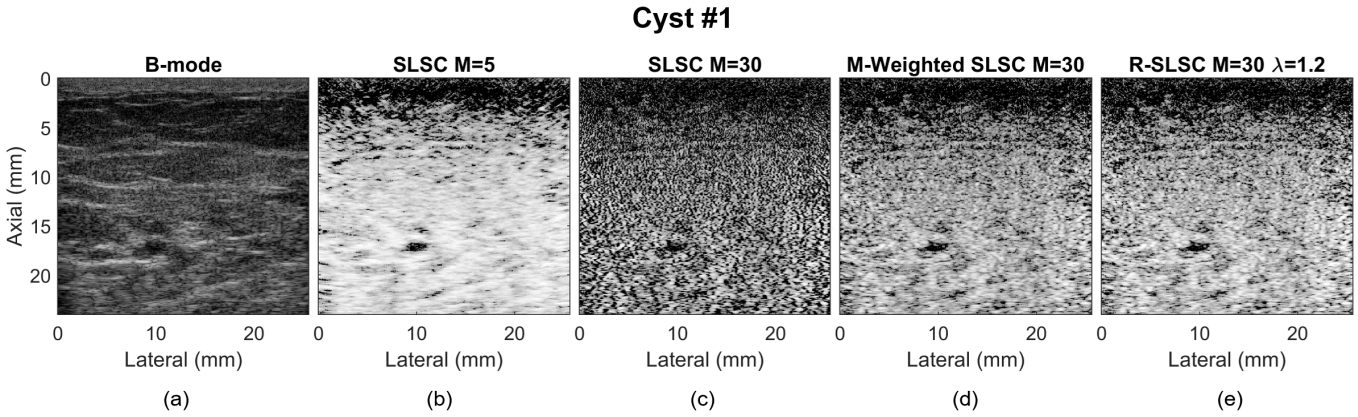

Fig. 1. Matched (a) B-mode, (b) SLSC $M = 5$, (c) SLSC $M = 30$, (d) M-Weighted SLSC, and (e) R-SLSC ($\lambda = 1.2$ and $M = 30$) images of an *in vivo* simple cyst in a female breast (referred to as Cyst #1). All images are displayed with 60-dB dynamic range. The dark region at the top of each type of SLSC image exists because we are using focused transmissions.

Although this selection process did not include CNR, we report it as a quantitative metric because it was previously shown that these three image quality metrics (contrast, CNR, and SNR) help to form a more holistic, quantitative perspective of ultrasound image quality improvements across multiple advanced beamforming methods [12]–[15], [26]. Note that our chosen selection process can be modified to replace contrast with resolution as the secondary metric in Step 2. In this alternative approach, Step 1 would still select R-SLSC images that match B-mode speckle SNR, and Step 2 would consider images with the most lags, resulting in images that theoretically include the most high-frequency information.

2) Kernel Size: When solving Equation (1), there is a choice in the length of the kernel k to be used. As the kernel length increases, the average in Equation (1) is taken over additional pixels, resulting in additional smoothing, improving contrast, CNR, and SNR. In simulations, Hyun *et al*. [27] and Bell *et al*. [17] showed that slightly increasing the kernel length beyond the typical value of one wavelength causes a linear increase in contrast and a minimal decrease in the axial resolution. The improved contrast, CNR, and SNR coupled with the minimal decrease in the axial resolution make an increased kernel length favorable for R-SLSC imaging. The additional smoothing caused by the increased kernel length also allows for the inclusion of additional lags when matching the B-mode SNR (i.e., Step 1), which improves the lateral resolution. Considering these benefits, we performed our analyses of SLSC, M-Weighted SLSC, and R-SLSC images with a kernel length of 1.56 times the wavelength associated with the center frequency of each probe (i.e., seven samples for the L3–8 probe and five samples for the L8–17 probe).

D. Resolution Measurement

As mentioned in Section III-C.1, the R-SLSC parameters can be selected to match the B-mode SNR using either contrast or resolution as a secondary metric in Step 2. To quantify differences in resolution, a double sigmoid function was fit to a lateral profile through the center of Cyst #2 similar to the approach described in [28]. The profile was averaged over seven axial pixels (which correspond to 0.1 mm), and a nonlinear least-squares fitting procedure was used to estimate the parameters in the following equation:

$$s(x) = (s_o - s_i)\left(\frac{1}{1 + e^{\frac{x - x_1}{m_1}}}\right)\left(\frac{1}{1 + e^{\frac{-(x - x_2)}{m_2}}}\right) + s_i \quad (7)$$

where s_o and s_i are the signal outside and inside the cyst, respectively, x_1 and x_2 are the locations of the left and right boundaries of the cyst, respectively, and m_1 and m_2 represent the widths of the transition on each side of the cyst. Resolution was defined as the distance required for 20%–80% transition of the lateral profile

$$\bar{r}_{2080} = 2\ln(4)\bar{m} \quad (8)$$

where $\bar{m}$ represents the average transition distance on both sides of the cyst.

IV. Results

A. Simple Cysts

Matched B-mode, SLSC, M-Weighted SLSC, and R-SLSC images of a simple cyst are shown in Fig. 1. The anechoic appearance of the cyst in the B-mode image of Fig. 1(a) is expected because the cyst is fluid filled. The SLSC image shown in Fig. 1(b) appears to contain less clutter than the original B-mode image, and the differences in tissue echogenicity surrounding the cyst are reduced in the SLSC images. Fig. 1(b) was chosen as an example of a good SLSC image because it is the lowest short-lag value ($M = 5$) with the best contrast [13]. Qualitatively, the contrast is high, and the cyst is prominent from the smoothed background, but due to the low-lag value, the resolution suffers. Fig. 1(c) shows the inclusion of additional lags, with $M = 30$. The resolution improves compared to Fig. 1(b) where $M = 5$, but the contrast, SNR, and CNR are significantly worse. Keeping the same lag value ($M = 30$) and using M-Weighted SLSC beamforming shown in Fig. 1(d), contrast is improved relative to Fig. 1(c) due to the larger weight on the short lags while also retaining the high-frequency information from the larger lag values. Finally, by applying R-SLSC beamforming, a majority of neighboring coherence outliers were removed shown in Fig. 1(e), resulting

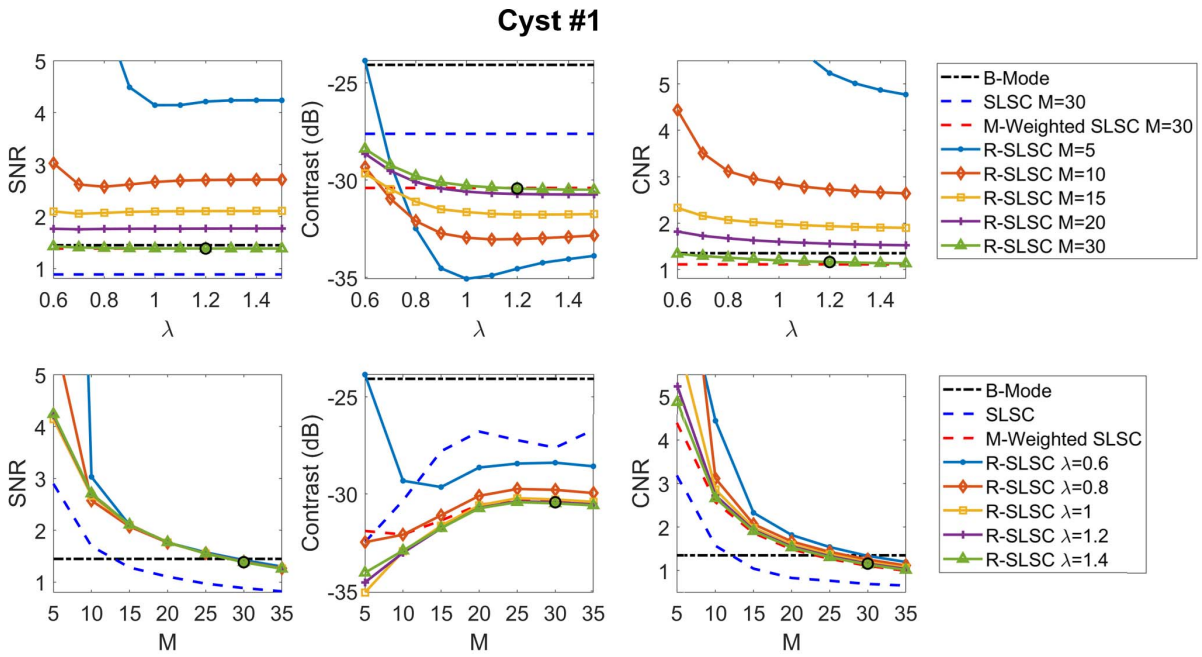

Fig. 2. Cyst #1 SNR, contrast, and CNR calculated for each B-Mode, SLSC, M-Weighted SLSC, and R-SLSC image. These metrics were calculated as functions of the sparsity parameter λ (top row) and the short-lag value M (bottom row). The circles indicate the values chosen to display the R-SLSC image shown in Fig. 1 ($\lambda = 1.2$ and $M = 30$).

in similar improvements to M-Weighted SLSC beamforming, with improved contrast and CNR when compared to the SLSC image at the same lag value ($M = 30$). In addition, R-SLSC imaging enables tuning of the tissue SNR to quantitatively match the speckle SNR of the B-mode image although the images are not an exact match qualitatively.

Fig. 2 shows the tissue SNR, contrast, and CNR of the cyst, plotted as a function of λ in the top row and as a function of M in the bottom row. The selected parameters used to display the R-SLSC image shown in Fig. 1(e) are indicated by circles around each data point. In general, SLSC, M-Weighted SLSC, and R-SLSC images demonstrate improved contrast, SNR, and CNR over the B-mode image particularly at low lags. As additional lags are considered, there are more coherence outliers, allowing a larger penalty, λ, to be imposed on those outliers. By tuning λ, we are able to quantitatively match the B-mode speckle SNR while retaining improved contrast. Note that this quantitative matching is beneficial because it increases the SNR that would, otherwise, be achieved with an SLSC image created with the same M-value. For example, this trend can be seen in Fig. 2 (top left), where the SNR of the SLSC image created with $M = 30$ is consistently lower than the selected R-SLSC parameters. When comparing M-Weighted SLSC to R-SLSC imaging, the contrast results shown in Fig. 2 agree with the results in [19]. In particular, the majority of the improvements in contrast with R-SLSC imaging compared to traditional SLSC images created with the same M-value are caused by the M-weighting step.

The qualitative descriptions above regarding cyst contrast, SNR, and CNR shown in Fig. 1 are similarly confirmed by the quantitative contrast measurements shown in Fig. 2. For example, the displayed B-mode, SLSC ($M = 30$), M-Weighted SLSC, and R-SLSC images achieve contrasts of -24.08, -27.62, -30.41, and -30.43 dB, respectively, demonstrating a 6.35-dB improvement in contrast from the initial B-mode image to the R-SLSC image.

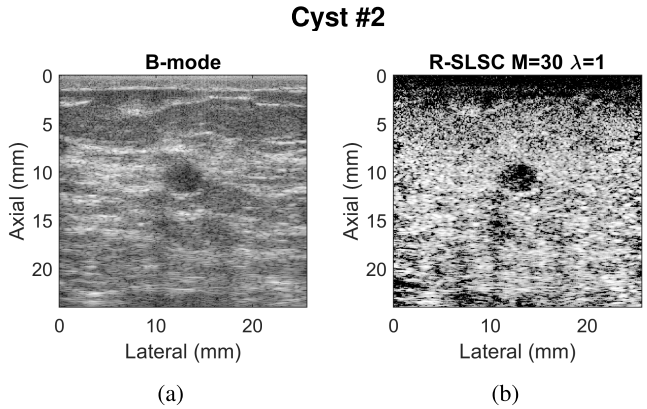

Fig. 3. Matched (a) B-mode and (b) R-SLSC images of an *in vivo* cyst in a female breast (displayed with 60-dB dynamic range).

The speckle SNR of the B-mode image was 1.45 (with an ROI chosen to best represent the tissue texture), which was used to select the R-SLSC image with a tissue SNR of 1.38 (as indicated by the circle shown in Fig. 2). At the same M value, the M-Weighted SLSC image has a similar tissue SNR of 1.38, and the original SLSC image ($M = 30$) has an even lower tissue SNR of 0.88. The CNRs at the selected M value for R-SLSC, M-Weighted SLSC, and B-mode images are similar (i.e., 1.35, 1.16, and 1.16, respectively). Additional image quality metrics for the images displayed in Fig. 1 are summarized in Table II.

Fig. 3 demonstrates a second example of a larger cyst with similar results. The measured contrast of the B-mode

TABLE II
IMAGE QUALITY METRICS

			Contrast (dB)	SNR	CNR
Fluid-filled Masses	Cyst #1	B-mode	-24.08	1.45	1.35
		SLSC M=5	-32.49	2.89	3.19
		SLSC M=30	-27.62	0.88	0.69
		M-Weighted	-30.41	1.38	1.16
		R-SLSC	-30.43	1.38	1.16
	Cyst #2	B-mode	-19.78	1.22	1.17
		SLSC M=5	-25.14	2.35	2.43
		SLSC M=30	-18.56	0.84	0.83
		M-Weighted	-22.31	1.24	1.28
		R-SLSC	-22.31	1.31	1.30
	Complicated Cyst	B-mode	-13.37	1.52	1.24
		SLSC M=5	-15.70	3.08	1.79
		SLSC M=30	-13.34	0.94	0.58
		M-Weighted	-14.99	1.45	0.89
		R-SLSC	-14.98	1.47	0.91
	Hematoma	B-mode	-18.15	1.76	1.53
		SLSC M=5	-19.34	3.46	2.78
		SLSC M=25	-19.54	1.11	0.98
		M-Weighted	-19.77	1.74	1.51
		R-SLSC	-19.69	1.80	1.55
Solid Masses	Fibroadenoma #1	B-mode	-14.65	1.41	1.13
		SLSC M=5	-1.93	1.83	0.29
		SLSC M=15	-1.54	1.06	0.13
		M-Weighted	-1.80	1.47	0.21
		R-SLSC	-1.73	1.50	0.21
	Fibroadenoma #2	B-mode	-11.71	1.40	0.48
		SLSC M=5	-3.91	2.00	0.71
		SLSC M=20	-3.59	0.95	0.30
		M-Weighted	-3.71	1.40	0.45
		R-SLSC	-3.60	1.42	0.46
	Complex Cystic and Solid Mass	B-mode	-9.56	1.30	1.06
		SLSC M=5	-4.17	2.26	0.66
		SLSC M=30	-4.13	0.86	0.27
		M-Weighted	-4.23	1.26	0.38
		R-SLSC	-4.14	1.29	0.38
	IDC	B-mode	-8.55	1.15	0.68
		SLSC M=5	-2.13	2.00	0.32
		SLSC M=25	-1.75	0.86	0.12
		M-Weighted	-1.90	1.23	0.18
		R-SLSC	-1.86	1.24	0.18
	DCIS	B-mode	-10.30	1.34	0.89
		SLSC M=5	-4.92	2.71	0.82
		SLSC M=30	-4.94	0.87	0.31
		M-Weighted	-4.99	1.30	0.45
		R-SLSC	-4.84	1.36	0.46

image displayed in Fig. 3(a) is −19.78 dB. The contrast of the displayed R-SLSC image (formed with $M = 30$ and $\lambda = 1$) is −22.31 dB, indicating an improvement of 2.53 dB in contrast. Qualitatively, the clutter in this cyst is reduced with the R-SLSC imaging. Additional image quality metrics are reported in Table II, where this second cyst is referred to as Cyst #2.

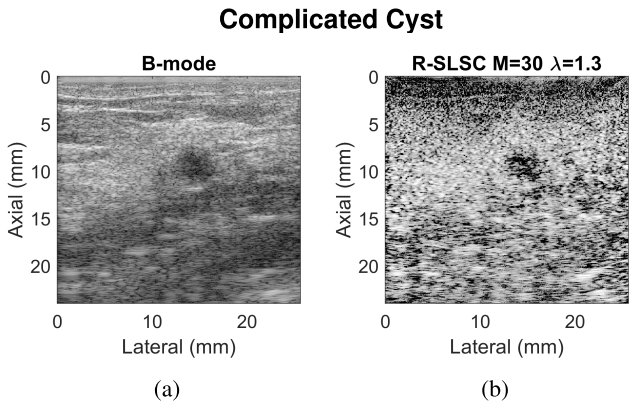

Fig. 4. Matched (a) B-mode and (b) R-SLSC images of an *in vivo* complicated cyst in a female breast (displayed with 60-dB dynamic range).

B. Complicated Cyst

Fig. 4 demonstrates a complicated cyst, which contains thicker fluid and internal "debris" compared to a simple cyst and, therefore, appears hypoechoic in B-mode images [29]. Qualitatively, the cysts shown in Figs. 3(a) and 4(a) look similar both having a hypoechoic appearance, potentially obscured by acoustic clutter. Examining the R-SLSC image shown in Fig. 4(b), the mass is not well circumscribed, particularly when compared to the circumscribed mass shown in Fig. 3(b) with R-SLSC imaging. Otherwise, it is clear from both examples [Figs. 3(b) and 4(b)] that the center of each cyst has low coherence.

Quantitatively, the contrast of the B-mode image displayed in Fig. 4(a) is −13.37 dB. The contrast of the displayed R-SLSC image (formed with $M = 30$ and $\lambda = 1.3$) is −14.98 dB, indicating an improvement of 1.61 dB in contrast. Additional image quality metrics are reported in Table II.

C. Hematoma

Matched B-mode, SLSC, M-Weighted SLSC, and R-SLSC images of the hematoma are shown in Fig. 5. A hematoma is generally a pool of blood, and blood has already been shown to produce low coherence (i.e., appear as a dark region in SLSC images) [13], [15], [18]. Fig. 5(a) shows the B-mode image displayed with 45-dB dynamic range. Fig. 5(b) shows an example of a good SLSC image because it is the lowest short-lag value ($M = 5$) with the best contrast, without suffering from significantly decreased SNR and CNR [13]. The contrast is high but at the expense of resolution as evidenced by observing the left edge of the hematoma. Fig. 5(c) demonstrates improved resolution with the inclusion of higher lags ($M = 25$) as the boundaries of the hematoma are more consistent with the B-mode image. However, the tissue SNR is significantly worse. Because of its size, the hematoma can still be clearly visualized in Fig. 5(c), but quantitatively the contrast is also worse in Fig. 5(c) when compared to that of Fig. 5(b) where $M = 5$. Using the same number of lags ($M = 25$), Fig. 5(d) shows improved contrast with M-Weighted SLSC imaging. Similarly, Fig. 5(e) demonstrates the ability of R-SLSC imaging to remove coherence outliers

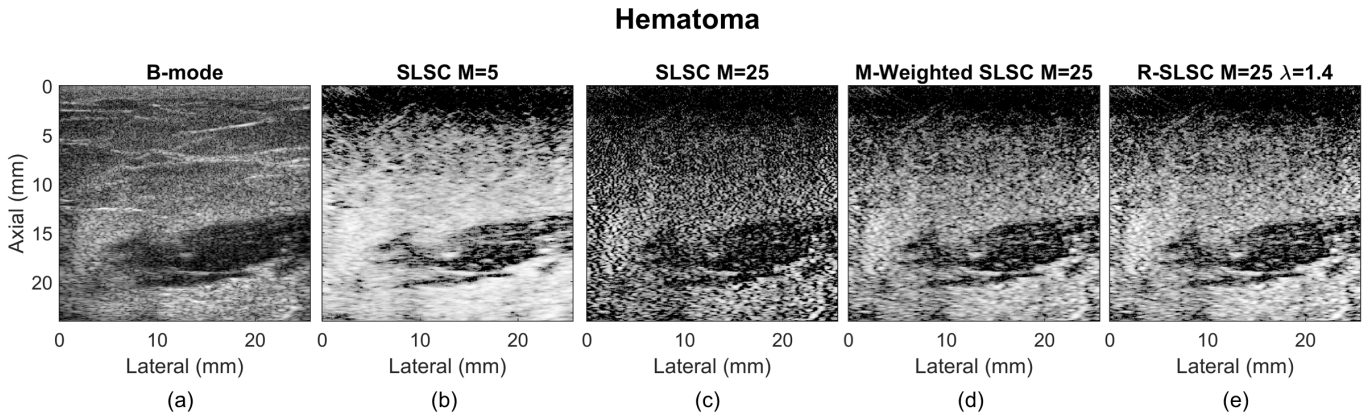

Fig. 5. Matched (a) B-mode, (b) SLSC $M = 5$, (c) SLSC $M = 25$, (d) M-Weighted SLSC, and (e) R-SLSC ($\lambda = 1.4$ and $M = 25$) images of an *in vivo* hematoma in a female breast displayed with 45-dB dynamic range. The dark region at the top of each type of SLSC image exists because we are using focused transmissions.

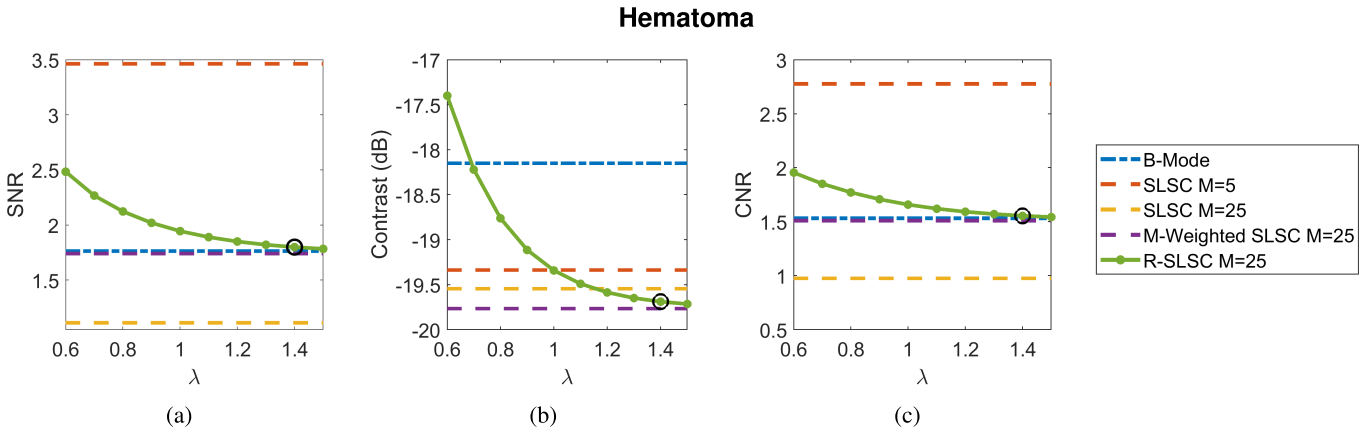

Fig. 6. Hematoma (a) SNR, (b) contrast, and (c) CNR calculated for each B-Mode, SLSC, M-Weighted SLSC, and R-SLSC image displayed as a function of the sparsity parameter λ. The circles indicate the values chosen to display the R-SLSC image shown in Fig. 5 ($\lambda = 1.4$ and $M = 25$).

and improve image contrast when compared to the matching SLSC image shown in Fig. 5(c) (created with $M = 25$). Fig. 5(e) shows the improved contrast and the best tradeoff between contrast and resolution while matching the speckle SNR of the B-mode image.

Fig. 6 demonstrates the contrast, SNR, and CNR of the hematoma. In Fig. 6, the selected parameters used to display the R-SLSC image of Fig. 5 are indicated by a circle around each data point. The contrast measurements for the displayed B-mode, SLSC ($M = 25$), M-Weighted SLSC, and R-SLSC images were -18.15, -19.54, -19.77, and -19.69 dB, respectively. Similar to the cyst, there is a 1.54-dB improvement in contrast between the B-mode image and the R-SLSC image. Table II summarizes these and other image quality metrics for the images of the hematoma displayed in Fig. 5.

D. Fibroadenomas

Matched B-mode, SLSC, M-Weighted SLSC, and R-SLSC images of one fibroadenoma are shown in Fig. 7. Typically, in RF channel data from anechoic and hypoechoic regions (representative of the cyst and hematoma, respectively), off-axis echoes from tissue are added deconstructively to the echoes from the hypoechoic region, resulting in low coherence within the hypoechoic region [12], [13], [15], [17]. However, the SLSC image of the fibroadenoma represents a departure from the typical appearance of hypoechoic regions in SLSC images to date. In the associated clinical notes, the fibroadenoma was identified as an "oval, circumscribed, parallel, and hypoechoic mass." The SLSC images show high coherence in this mass (i.e., similar coherence to surrounding tissue), which clarifies that this hypoechoic mass contains solid rather than fluid-filled cystic content.

An example of a good SLSC image is shown in Fig. 7(b) with $M = 5$ because it is the lowest short-lag value with the best (i.e., most negative) contrast. The edges of the fibroadenoma are visible, and the heterogeneous tissue surrounding the mass is smooth in the SLSC image. Fig. 7(c) shows an additional SLSC image including larger lags ($M = 15$). This image shows significantly lower SNR when compared to the SLSC image formed with $M = 5$ [Fig. 7(b)], which reduces the detectability of the fibroadenoma. Including the same number of lags ($M = 15$), the M-Weighted SLSC

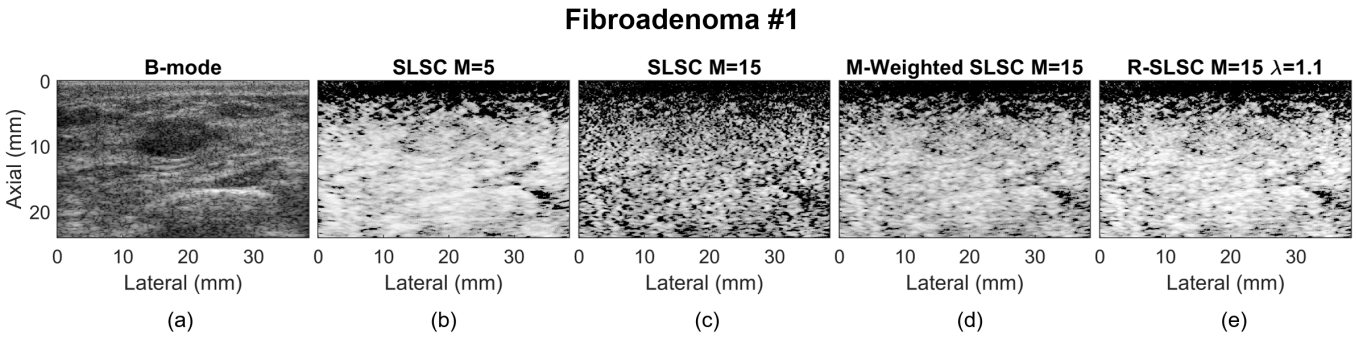

Fig. 7. Matched (a) B-mode, (b) SLSC $M = 5$, (c) SLSC $M = 15$, (d) M-Weighted SLSC, and (e) R-SLSC ($\lambda = 1.1$ and $M = 15$) images of an *in vivo* fibroadenoma in a female breast displayed with 60-dB dynamic range (referred to as fibroadenoma #1). The dark region at the top of each type of SLSC image exists because we are using focused transmissions.

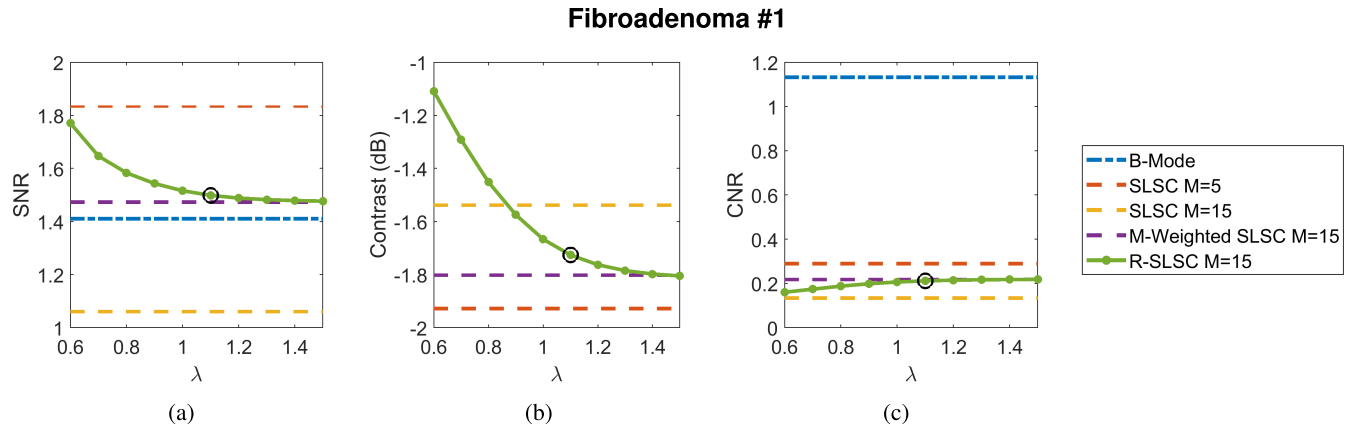

Fig. 8. Fibroadenoma #1 (a) SNR, (b) contrast, and (c) CNR calculated for each B-Mode, SLSC, M-Weighted SLSC, and R-SLSC image displayed as a function of the sparsity parameter λ. The circles indicate the values chosen to display the R-SLSC image shown in Fig. 7 ($\lambda = 1.1$ and $M = 15$).

image [i.e., Fig. 7(d)] and R-SLSC image shown in Fig. 7(e) display better border delineation than their traditional SLSC counterpart [i.e., Fig. 7(c)].

Fig. 8 shows contrast, tissue SNR, and CNR measurements. In Fig. 8, the selected parameters used in the R-SLSC image of Fig. 7 are indicated by a circle around each data point. Because the fibroadenoma presents as hypoechoic, we expect the contrast in the B-mode image to be good. The measured contrast in the B-mode image was -14.65 dB. The contrasts of the SLSC ($M = 15$), M-Weighted SLSC ($M = 15$), and R-SLSC ($M = 15$ and $\lambda = 1.1$) images were significantly worse, measuring -1.54, -1.80, and -1.73 dB, respectively. Because of the large difference in contrast, the B-mode contrast was excluded from Fig. 8 in order to better visualize the changes in various SLSC imaging methods. The clinical significance of this finding is discussed in detail in Section V-A. The image quality metrics for the images displayed in Fig. 7 are summarized in Table II. As expected, the CNR of the fibroadenoma in the SLSC, M-Weighted SLSC, and R-SLSC images are all <0.3 due to the internal coherence. The tissue SNRs of the SLSC, M-Weighted SLSC, and R-SLSC images are 1.06, 1.47, and 1.50, respectively.

Fig. 9 demonstrates a second example of a fibroadenoma with similar results. The B-mode image displayed in Fig. 9(a) has a contrast of -11.71 dB, while the R-SLSC image (formed with $M = 20$ and $\lambda = 1.2$) has a contrast of -3.60 dB, suggesting solid content inside of the mass. Additional image quality metrics for this fibroadenoma are reported in Table II.

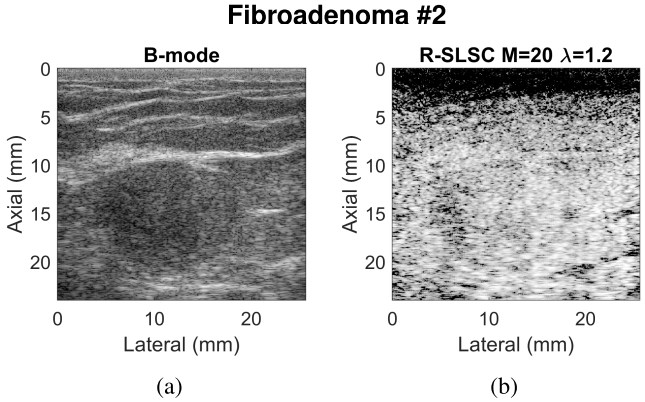

Fig. 9. Matched (a) B-mode and (b) R-SLSC images of an *in vivo* fibroadenoma in a female breast displayed with 60-dB dynamic range.

E. Complex Cystic and Solid Mass

Matched B-mode and R-SLSC images of the complex cystic and solid mass are shown in Fig. 10. Specifically, the pathological finding for this mass was fibrocystic changes including apocrine metaplasia and columnar cell change.

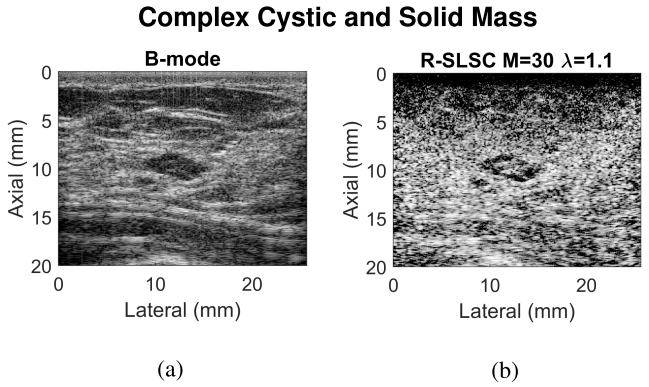

Fig. 10. Matched (a) B-mode and (b) R-SLSC images of an *in vivo* complex cystic and solid mass in a female breast displayed with 45-dB dynamic range.

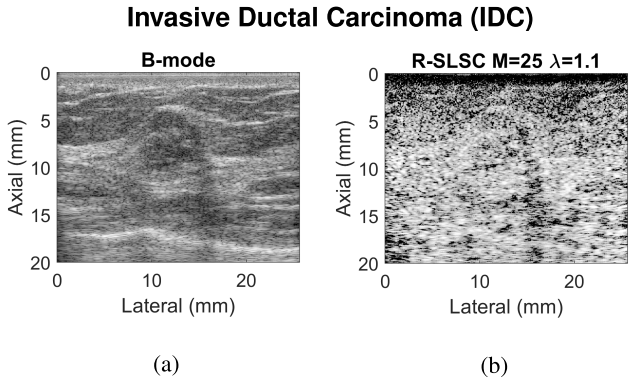

Fig. 11. Matched (a) B-mode and (b) R-SLSC images of an *in vivo* IDC in a female breast displayed with 60-dB dynamic range.

The R-SLSC image was formed with $\lambda = 1.1$ and $M = 30$. Both images are displayed with a dynamic range of 45 dB to facilitate comparisons between the B-mode and the R-SLSC image. Table II summarizes the image quality metrics for this complex cystic and solid mass. Specifically, the contrasts of the B-mode, SLSC ($M = 30$), M-Weighted SLSC ($M = 30$), and R-SLSC ($M = 30$) images were -9.56, -4.13, -4.23, and -4.14 dB, respectively. Similar to the fibroadenoma, the coherence inside of the mass causes a significantly greater contrast in the B-mode image than in the R-SLSC image, accentuating the solid content within the cystic structure.

F. Carcinomas

Matched B-mode and R-SLSC images of an IDC are shown in Fig. 11. The R-SLSC image was formed with $\lambda = 1.1$ and $M = 25$. Both images are displayed with a dynamic range of 60 dB. Table II summarizes the image quality metrics for this IDC. Specifically, the contrasts of the B-mode, SLSC ($M = 25$), M-Weighted SLSC ($M = 25$), and R-SLSC ($M = 25$) images were -8.55, -1.75, -1.90, and -1.86 dB, respectively. The IDC appears somewhat hypoechoic in the B-mode image, but similar to the fibroadenoma, the coherence inside of the mass results in poorer contrast in the R-SLSC image when compared to the B-mode image, suggesting that the mass is solid.

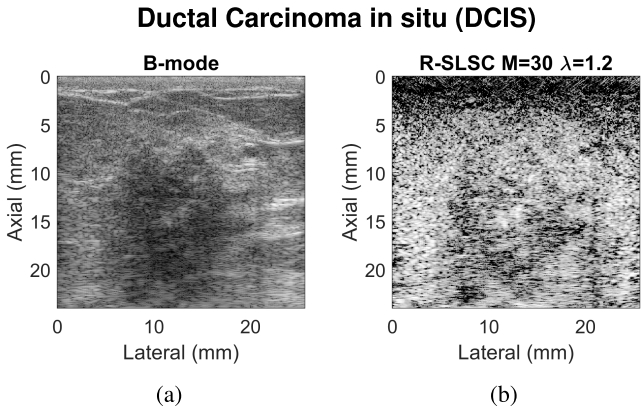

Fig. 12. Matched (a) B-mode and (b) R-SLSC images of an *in vivo* DCIS in a female breast displayed with 60-dB dynamic range.

Similarly, Fig. 12 shows the matched B-mode and R-SLSC images of a DCIS, which was determined based on the core-needle biopsy results. The R-SLSC image was formed with $\lambda = 1.2$ and $M = 30$. Both images are displayed with a dynamic range of 60 dB. The contrasts of the mass in the B-mode, SLSC ($M = 30$), M-Weighted SLSC ($M = 30$), and R-SLSC ($M = 30$ and $\lambda = 1.2$) images were -10.30, -4.94, -4.98, and -4.84 dB, respectively. Table II summarizes these and other image quality metrics for this DCIS. The DCIS appears somewhat hypoechoic in the B-mode image, but similar to the fibroadenoma and the IDC, the coherence inside of the mass results in poorer contrast in the R-SLSC image than in the B-mode image, suggesting that the mass is solid.

G. Differentiating Fluid-Filled From Solid Hypoechoic Masses Based on Coherence Information

Our initial clinical application of SLSC, M-Weighted SLSC, and R-SLSC imaging to breast data led us to observe that these SLSC imaging methods could be a viable approach to distinguish fluid-filled from solid hypoechoic masses. The quantitative feature that best shows this distinction is the contrast measurement. A summary comparison of the contrast between solid and fluid-filled masses is visually displayed in Fig. 13 where the blue-shaded region contains fluid-filled masses and the gray-shaded region indicates solid masses. The box-and-whisker plots show the median (horizontal line) and the upper and lower quartiles of each data set (upper and lower edges of each box). Each data set consists of 10 frames of RF data from the same mass. The top and bottom lines of the whiskers indicate the maximum and minimum of each data set, and the crosses indicate any outliers (defined as any contrast larger than 1.5 times the interquartile range). Fluid-filled regions demonstrate comparable contrast between B-mode and each SLSC image. On the other hand, the coherence-based images of each solid lesion demonstrate significantly worse contrast when compared to each corresponding B-mode image, as verified using a repeated measures ANOVA ($p < 0.001$). These results highlight the ability of SLSC, M-Weighted SLSC, and R-SLSC imaging to better display solid content within breast masses based solely on the contrast information.

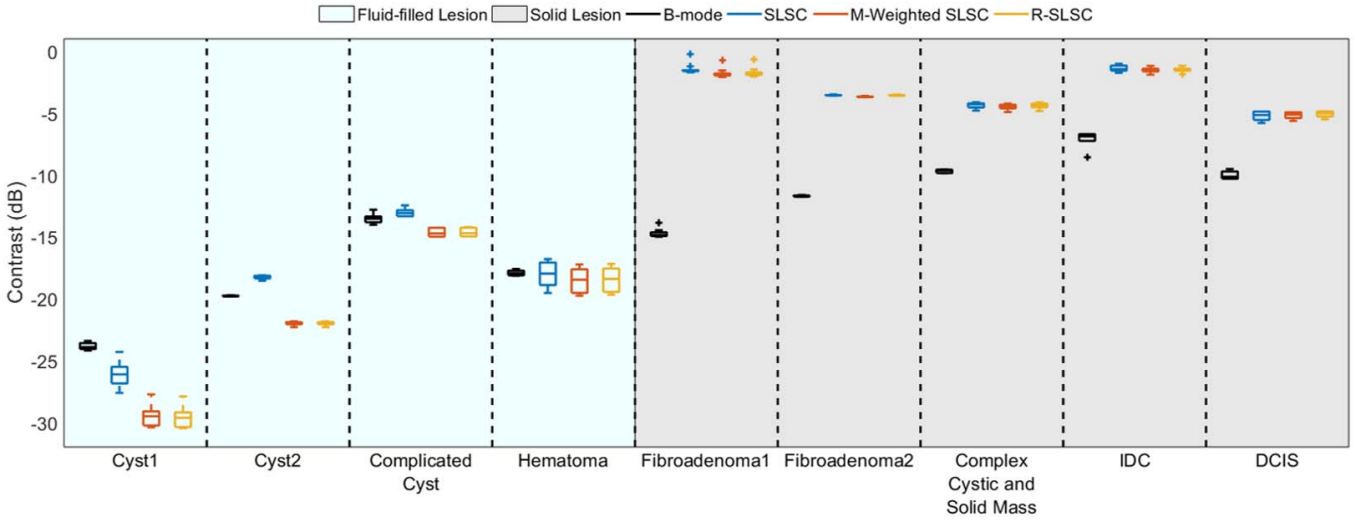

Fig. 13. Comparison of contrast measurements between each of the four images (i.e., B-Mode, SLSC, M-Weighted SLSC, and R-SLSC). Blue-shaded regions: fluid-filled masses. Gray-shaded regions: solid lesions. Each fluid-filled lesion has similar or better contrast when the coherence-based imaging methods are compared to each respective B-mode image. On the other hand, each solid lesion has significantly worse contrast ($p < 0.001$) when the coherence-based imaging methods are compared to each respective B-mode image.

Generally, contrast values above -6 dB in the coherence-based images indicate the presence of a solid mass.

H. Effect of Resolution-Based R-SLSC Selection Parameters

As mentioned in Section III-C1, the parameters for R-SLSC imaging throughout this paper were selected with contrast as the secondary metric. This metric was chosen considering our primary goal of demonstrating the potential of coherence-based imaging methods to differentiate between fluid-filled and solid masses. One additional benefit of R-SLSC beamforming over M-Weighted SLSC beamforming is the ability to include higher lags while matching the B-mode speckle SNR. For the masses presented throughout this paper, the alternative Step 2 described in Section III-C.1 results in an average of 8.6% more lags included in the R-SLSC image when compared to the M-Weighted SLSC image at a similar tissue SNR to the B-mode image. The method described in Section III-D was used to quantify the resolution of Cyst #2 to demonstrate this trend.

Fig. 14 shows a lateral profile through Cyst #2 averaged over seven pixels (0.1 mm) in the axial dimension, where the colored dashed lines indicate the double sigmoid fit applied to each beamforming method. Fig. 14 (bottom) shows a zoomed in view of the right edge of the cyst profile. Visualizing the transition length of each sigmoid fit, the SLSC curve has the longest transition, followed by the M-Weighted SLSC curve, and finally the R-SLSC curve. The measured resolutions [i.e., $\bar{r}_{2080}$ in Equation (8)] for SLSC ($M = 5$), M-Weighted SLSC ($M = 30$), and R-SLSC ($M = 35$) are 1.21, 0.04, and 0.02 mm, respectively, demonstrating 50% improved resolution of R-SLSC imaging over M-Weighted SLSC imaging when additional lags are included.

Note that this improvement in the lateral resolution is often achieved at the expense of contrast. For example, when using contrast as the secondary metric to select our R-SLSC parameters for displaying the hematoma, the contrasts of the resulting image (at $M = 25$ and $\lambda = 1.4$) are -19.7 dB. Alternatively, when using resolution as the secondary metric to select the R-SLSC parameters, the contrast of the resulting image (at $M = 35$ and $\lambda = 0.6$) is -17.6 dB, which corresponds to a 2.1-dB degradation in contrast.

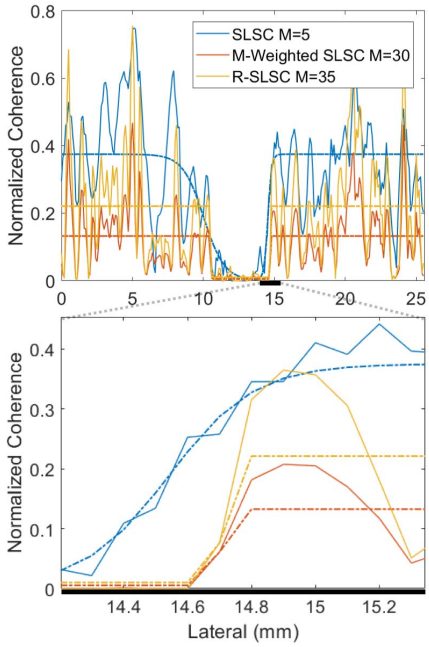

Fig. 14. Lateral profiles through Cyst #2 taken from the normalized image of each beamforming method and averaged across seven axial pixels (0.1 mm). The colored dashed lines indicate the double sigmoid fit function applied to each beamforming method. The top graph shows the full lateral profile, while the bottom graph shows a zoomed in section of the right-most edge of the cyst.

V. Discussion

A. Clinical Significance and Opportunities

The results presented in this paper indicate that there are four potential clinical advantages to applying SLSC, M-Weighted SLSC, and R-SLSC imaging to breast ultrasound data. First, SLSC imaging reduces clutter in fluid-filled targets (i.e., the cysts and the hematoma), resulting in improved target visibility when compared to corresponding ultrasound B-mode images. Target visibility is further improved by the application of M-Weighted SLSC imaging and R-SLSC imaging, which enables the most control of the tissue SNR due to the additional tissue smoothing achieved by increasing λ. When introduced in the clinic, these parameters can potentially be adjusted to each radiologist's preferences, similar to the dynamic range parameter on clinical scanners.

Second, the appearance of solid masses (such as the fibroadenomas, complex cystic and solid mass, IDC, and DCIS) in the SLSC images has potential clinical applications in distinguishing solid from fluid masses. For example, a fibroadenoma is a solid, palpable mass that often presents on B-mode images as hypoechoic [30], but with the B-mode image alone, the fibroadenoma might be confused for a large fluid-filled cyst containing acoustic clutter (due to its hypoechoic appearance). With the addition of SLSC imaging, clinicians could review the SLSC images alongside B-mode images to determine that this is not a cyst obscured by clutter, and it is instead a solid mass. This finding is further supported by the presentation of the complex cystic and solid mass, the IDC, and the DCIS.

One might attribute the coherent center of these solid masses to recorrelation, a known effect that was previously observed in simulated images. However, when noise was added to simulated images, this recorrelation effect was no longer present [12]. In addition, experimental SLSC images do not include this recorrelation effect due to the presence of expected thermal and electronic noises. Similarly, the solid masses shown in Figs. 7(a), 10(a), and 11(a) are large targets in comparison with the cyst, but because these scans were taken in a clinical setting, the recorrelation effect is not expected to cause the coherence that we observe inside each solid mass. Instead, the coherence is attributed to the spatially correlated content of the solid hypoechoic masses.

While improving the diagnostic accuracy for detecting benign hypoechoic fibroadenomas as solid masses is important, making the distinction between benign and malignant lesions would have additional clinical significance, which is the third potential advantage of SLSC, M-Weighted SLSC, and R-SLSC imaging. For example, high-grade IDC of the breast typically presents as hypoechoic on B-mode and often looks very similar to complicated cysts [31], [32]. As the IDC presented in Fig. 11 appears somewhat hypoechoic, our results suggest the potential of SLSC, M-Weighted SLSC, and R-SLSC imaging to assist with distinguishing IDCs that appear similar to cysts. Therefore, an additional benefit of these coherence-based imaging methods is their potential to reduce the current false positive rates that are greater than 30% with ultrasound imaging [33]. For complicated cysts specifically, in a study by Berg *et al*. [29], of 296 complicated cyst detected with ultrasound, 135 were designated as "probably benign" and 28 were designated as having suspicious features, requiring follow up, aspiration, or biopsy, with only two resulting cancers, yielding a false positive rate of 93%. If SLSC, M-Weighted SLSC, and/or R-SLSC imaging could have identified the two cancers as solid masses and the others as cystic, then the remaining masses could have been more confidently diagnosed as benign and spared from follow up, thus reducing the false positive rates. A reduction in the false positives detected by ultrasound can lead to fewer breast biopsies returned as benign and reduce patient anxiety as well as the number of burdensome patient follow-up procedures that place a strain on the overall resources of our health care system.

Finally, the fourth clinical advantage can potentially be achieved with R-SLSC imaging by tuning λ to further enhance resolution (see Fig. 14). The improved resolution may have clinical significance in future resolution-dependent applications, such as microcalcification detection.

B. Clinical Challenges

We have demonstrated that in hypoechoic and anechoic regions, SLSC images generally provide improvements in contrast when compared to their B-mode counterparts. However, the resulting SLSC breast images have tissue texture that is not familiar to clinicians when compared to that of traditional ultrasound images, which creates unique challenges for the widespread clinical acceptance of SLSC imaging. Traditional ultrasound B-mode images contain a standard speckle pattern that is familiar to clinicians and often has diagnostic significance. When choosing images to display, R-SLSC images allow the speckle pattern to be taken into account by varying λ, attempting to match tissue SNR to that of traditional B-mode images. When coherence-based images with a higher SNR were presented to our radiologist co-authors (Kelly Myers and Eniola Falomo), these images were considered "too harsh," and the image was assumed to be improperly tuned based on the previous experience and training with reading breast ultrasound images. Although equivalent values of tissue SNR in SLSC images and B-mode images do not produce the same tissue texture appearance, tissue SNR, nonetheless, provides a metric to quantitatively compare the two images. Our initial exploration indicates that R-SLSC images with matched SNRs to B-mode images provide the best tradeoff among clinician familiarity, contrast, and resolution.

Another known challenge is that SLSC imaging is more computationally intensive than delay-and-sum beamforming, making its translation into the clinic more difficult, but increasingly possible with GPU processing [34]. In addition, the dark region observed at the top of many of the SLSC and R-SLSC images can be resolved with synthetic aperture imaging [35], which will further increase computation

times. R-SLSC imaging similarly provides additional computational complexity, but Nair *et al.* [19] presents two additional methods that could be used to parallelize this computation by performing the RPCA step on sections of the image at a time.

Finally, the SLSC image alone is not sufficient to definitively provide a diagnosis, particularly in situations where a solid mass has internal coherence that is similar to the coherence of surrounding tissue. This distinction is further confounded by the smoothing step introduced with M-Weighted and R-SLSC imaging. Because the background tissue texture may provide additional information to clinicians, we propose SLSC, M-Weighted SLSC, and/or R-SLSC imaging to be used in parallel or as a duplex mode to the B-mode imaging, providing clinicians with the option to switch between B-mode and SLSC imaging, as demonstrated in [36]. This added feature has potential to provide either further insight into the presence of solid mass contents or clutter reduction in fluid-filled hypoechoic masses.

VI. Conclusion

This work is the first to investigate the application of SLSC imaging to breast ultrasound data. Quantitative image quality metrics showed improved contrast in hypoechoic cysts and hematoma targets. These metrics were further improved with M-Weighted SLSC and R-SLSC imaging. By varying λ and smoothing tissue texture, R-SLSC imaging enables us to display tissue SNR that is quantitatively similar to traditional ultrasound speckle SNR. Therefore, the resulting image has a tissue texture that is preferred by trained radiologists (although differences in the surrounding tissue echogenicity are no longer evident in the SLSC breast images when compared to the B-mode images). In addition, the high coherence inside of solid masses suggests the capability of SLSC, M-Weighted SLSC, and R-SLSC imaging to aid in the distinction between solid and fluid-filled masses, which could potentially lead to distinctions between complicated cysts and high-grade IDCs, and reductions in the false positive rates of ultrasound imaging. Overall, our results highlight the potential for SLSC, M-Weighted SLSC, and R-SLSC imaging to improve the fluid versus solid classification of hypoechoic breast masses and improve the detectability of fluid-filled masses, thereby improving the diagnostic power of breast ultrasound imaging.

Appendix

In order to facilitate comparisons between the B-mode images and each SLSC image, the ROIs are not shown in the main body of this paper. For reference, Fig. 15 shows the ROIs used for quantitative image quality metrics. The white box indicates the regions chosen for contrast and CNR. For the masses where the outside ROI was small, the larger ROI indicated by the yellow dashed box was used for SNR calculations. Otherwise, the white box outside of the mass was used to calculate SNR.

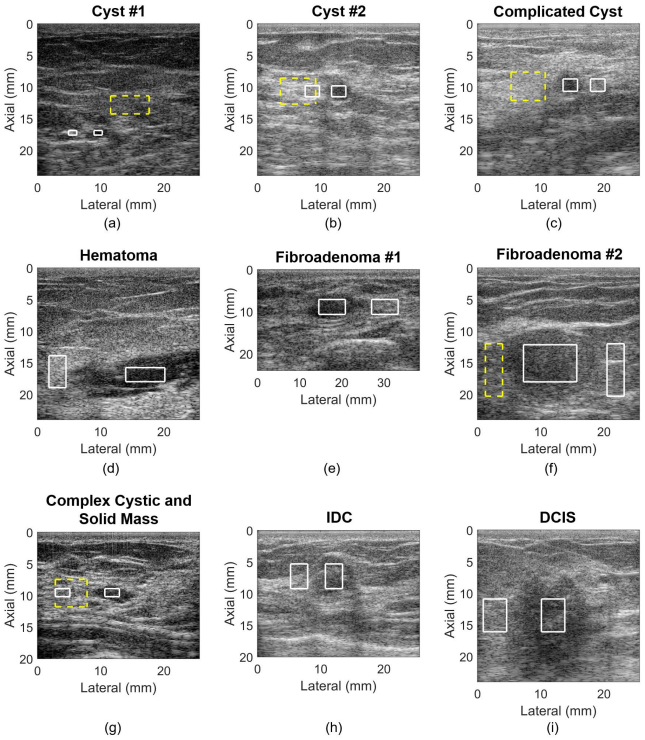

Fig. 15. ROI for each mass presented. (a) Cyst #1. (b) Cyst #2. (c) Complicated Cyst. (d) Hematoma. (e) Fibroadenoma #1. (f) Fibroadenoma #2. (g) Complex cystic and solid mass. (h) IDC. (i) DCIS. White box: ROI used for contrast and CNR calculations. For the masses where the outside ROI was small, the larger ROI indicated by the yellow dashed box was used for SNR calculations. Otherwise, the white box outside of the mass was used to calculate SNR.

Acknowledgment

The authors thank A. Nair for his help with setting up and debugging the original Robust SLSC code.

References

[1] R. L. Siegel, K. D. Miller, and A. Jemal, "Cancer statistics, 2018," *CA, Cancer J. Clin.*, vol. 68, no. 1, pp. 7–30, Jan. 2018.

[2] D. A. Berry *et al.*, "Effect of screening and adjuvant therapy on mortality from breast cancer," *New England J. Med.*, vol. 353, no. 17, pp. 1784–1792, 2005.

[3] C. DeSantis, R. Siegel, P. Bandi, and A. Jemal, "Breast cancer statistics, 2011," *CA, Cancer J. Clinicians*, vol. 61, no. 6, pp. 408–418, 2011.

[4] M. T. Mandelson *et al.*, "Breast density as a predictor of mammographic detection: Comparison of interval- and screen-detected cancers," *J. Nat. Cancer Inst.*, vol. 92, no. 13, pp. 1081–1087, 2000.

[5] M. A. Lediju, M. J. Pihl, J. J. Dahl, and G. E. Trahey, "Quantitative assessment of the magnitude, impact and spatial extent of ultrasonic clutter," *Ultrason. Imag.*, vol. 30, no. 3, pp. 151–168, Jul. 2008.

[6] G. F. Pinton, G. E. Trahey, and J. J. Dahl, "Sources of image degradation in fundamental and harmonic ultrasound imaging using nonlinear, full-wave simulations," *IEEE Trans. Ultrason., Ferroelectr., Freq. Control*, vol. 58, no. 4, pp. 754–765, Apr. 2011.

[7] S. Huber, M. Wagner, M. Medl, and H. Czembirek, "Real-time spatial compound imaging in breast ultrasound," *Ultrasound Med. Biol.*, vol. 28, no. 2, pp. 155–163, 2002.

[8] R. Entrekin, P. Jackson, J. R. Jago, and B. A. Porter, "Real time spatial compound imaging in breast ultrasound: Technology and early clinical experience," *Medicamundi*, vol. 43, no. 3, pp. 35–43, 1999.

[9] M. van Wijk and J. M. Thijssen, "Performance testing of medical ultrasound equipment: Fundamental vs. harmonic mode," *Ultrasonics*, vol. 40, no. 1, pp. 585–591, 2002.

[10] S.-L. Wang, C.-H. Chang, H.-C. Yang, Y.-H. Chou, and P.-C. Li, "Performance evaluation of coherence-based adaptive imaging using clinical breast data," *IEEE Trans. Ultrason., Ferroelectr., Freq. Control*, vol. 54, no. 8, pp. 1669–1678, Aug. 2007.

[11] P.-C. Li and M.-L. Li, "Adaptive imaging using the generalized coherence factor," *IEEE Trans. Ultrason., Ferroelectr., Freq. Control*, vol. 50, no. 2, pp. 128–141, Feb. 2003.
[12] M. A. Lediju, G. E. Trahey, B. C. Byram, and J. J. Dahl, "Short-lag spatial coherence of backscattered echoes: Imaging characteristics," *IEEE Trans. Ultrason., Ferroelect., Freq. Control*, vol. 58, no. 7, pp. 1377–1388, Jul. 2011.
[13] M. A. L. Bell, R. Goswami, J. A. Kisslo, J. J. Dahl, and G. E. Trahey, "Short-lag spatial coherence imaging of cardiac ultrasound data: Initial clinical results," *Ultrasound Med. Biol.*, vol. 39, no. 10, pp. 1861–1874, 2013.
[14] V. Kakkad, J. Dahl, S. Ellestad, and G. Trahey, "*In vivo* application of short-lag spatial coherence and harmonic spatial coherence imaging in fetal ultrasound," *Ultrason. Imag.*, vol. 37, no. 2, pp. 101–116, 2015.
[15] M. Jakovljevic, G. E. Trahey, R. C. Nelson, and J. J. Dahl, "*In vivo* application of short-lag spatial coherence imaging in human liver," *Ultrasound Med. Biol.*, vol. 39, no. 3, pp. 534–542, 2013.
[16] W. Long *et al.*, "Clinical utility of fetal short-lag spatial coherence imaging," *Ultrasound Med. Biol.*, vol. 44, no. 4, pp. 794–806, 2018.
[17] M. A. L. Bell, J. J. Dahl, and G. E. Trahey, "Resolution and brightness characteristics of short-lag spatial coherence (SLSC) images," *IEEE Trans. Ultrason., Ferroelectr., Freq. Control*, vol. 62, no. 7, pp. 1265–1276, Jul. 2015.
[18] J. J. Dahl, D. Hyun, M. Lediju, and G. E. Trahey, "Lesion detectability in diagnostic ultrasound with short-lag spatial coherence imaging," *Ultrason. Imag.*, vol. 33, no. 2, pp. 119–133, Apr. 2011.
[19] A. A. Nair, T. D. Tran, and M. A. L. Bell, "Robust short-lag spatial coherence imaging," *IEEE Trans. Ultrason., Ferroelectr., Freq. Control*, vol. 65, no. 3, pp. 366–377, Mar. 2018.
[20] R. Mallart and M. Fink, "The van Cittert–Zernike theorem in pulse echo measurements," *J. Acoust. Soc. Amer.*, vol. 90, no. 5, pp. 2718–2727, 1991.
[21] D.-L. Liu and R. C. Waag, "About the application of the van Cittert-Zernike theorem in ultrasonic imaging," *IEEE Trans. Ultrason., Ferroelectr., Freq. Control*, vol. 42, no. 4, pp. 590–601, Jul. 1995.
[22] J. A. Rice, *Mathematical Statistics and Data Analysis* (Advanced Series). Boston, MA, USA: Cengage Learning, 2006, p. 3.
[23] J. Wright, A. Ganesh, S. Rao, Y. Peng, and Y. Ma, "Robust principal component analysis: Exact recovery of corrupted low-rank matrices via convex optimization," in *Proc. Adv. Neural Inf. Process. Syst.*, 2009, pp. 2080–2088.
[24] Z. Lin, M. Chen, and Y. Ma. (2010). "The augmented lagrange multiplier method for exact recovery of corrupted low-rank matrices." [Online]. Available: https://arxiv.org/abs/1009.5055
[25] Z. Lin, M. Chen, and Y. Ma. *Low-Rank Matrix Recovery and Completion Via Convex Optimization*. Accessed: Nov. 28, 2017. [Online]. Available: http://perception.csl.illinois.edu/matrix-rank/sample_code.html
[26] S. M. Hverven, O. M. H. Rindal, A. Rodriguez-Molares, and A. Austeng, "The influence of speckle statistics on contrast metrics in ultrasound imaging," in *Proc. IEEE Int. Ultrason. Symp. (IUS)*, Sep. 2017, pp. 1–4.
[27] D. Hyun, A. L. C. Crowley, and J. J. Dahl, "Efficient strategies for estimating the spatial coherence of backscatter," *IEEE Trans. Ultrason., Ferroelectr., Freq. Control*, vol. 64, no. 3, pp. 500–513, Mar. 2017.
[28] N. C. Rouze, M. H. Wang, M. L. Palmeri, and K. R. Nightingale, "Parameters affecting the resolution and accuracy of 2-D quantitative shear wave images," *IEEE Trans. Ultrason., Ferroelectr., Freq. Control*, vol. 59, no. 8, pp. 1729–1740, Aug. 2012.
[29] W. A. Berg, A. G. Sechtin, H. Marques, and Z. Zhang, "Cystic breast masses and the acrin 6666 experience," *Radiologic Clinics*, vol. 48, no. 5, pp. 931–987, 2010.
[30] B. D. Fornage, J. G. Lorigan, and E. Andry, "Fibroadenoma of the breast: Sonographic appearance," *Radiology*, vol. 172, no. 3, pp. 671–675, 1989.
[31] A. H. Rotstein and P. K. Neerhut, "Ultrasound characteristics of histologically proven grade 3 invasive ductal breast carcinoma," *J. Med. Imag. Radiat. Oncol.*, vol. 49, no. 6, pp. 476–479, 2005.
[32] P. M. Lamb, N. M. Perry, S. J. Vinnicombe, and C. A. Wells, "Correlation between ultrasound characteristics, mammographic findings and histological grade in patients with invasive ductal carcinoma of the breast," *Clin. Radiol.*, vol. 55, no. 1, pp. 40–44, 2000.
[33] W. A. Berg, A. I. Bandos, E. B. Mendelson, D. Lehrer, R. A. Jong, and E. D. Pisano, "Ultrasound as the primary screening test for breast cancer: Analysis from ACRIN 6666," *J. Nat. Cancer Inst.*, vol. 108, no. 4, p. djv367, 2015.
[34] D. Hyun, G. E. Trahey, and J. Dahl, "A GPU-based real-time spatial coherence imaging system," *Proc. SPIE*, vol. 8675, p. 86751B, Mar. 2013.
[35] N. Bottenus, B. C. Byram, J. J. Dahl, and G. E. Trahey, "Synthetic aperture focusing for short-lag spatial coherence imaging," *IEEE Trans. Ultrason., Ferroelectr., Freq. Control*, vol. 60, no. 9, pp. 1816–1826, Sep. 2013.
[36] A. Wiacek *et al.*, "Clinical feasibility of coherence-based beamforming to distinguish solid from fluid hypoechoic breast masses," in *Proc. IEEE Int. Ultrason. Symp. (IUS)*, Oct. 2018.

Alycen Wiacek (S'13) received the B.S. degree in electrical and computer engineering (ECE) from Wayne State University, Detroit, MI, USA, in 2014, and the M.S. degree in ECE from Oakland University, Rochester, MI, USA, in 2015, with a focus on signal processing. She is currently pursuing the Ph.D. degree in ECE at Johns Hopkins University, Baltimore, MD, USA.

Her research interests include coherence-based imaging, breast ultrasound, and photoacoustic imaging.

Ole Marius Hoel Rindal (S'14) was born in Hamar, Norway, in 1990. He received the M.S. degree in computer science (signal processing) from the University of Oslo, Oslo, Norway, in 2014, where he is currently pursuing the Ph.D. degree in medical ultrasound beamforming techniques.

He also holds a position at the Centre for Elite Sports Research, Norwegian University of Science and Technology, Trondheim, Norway, where he is doing research on signal processing of the inertial measurement units used in cross-country skiing. His research interests include signal processing, medical image formation, image processing, machine learning, physiological, and biomechanical aspects of cross-country skiing.

Eniola Falomo received the M.D. degree from Northwestern University, Evanston, IL, USA, in 2008. She completed her residency at the University of Wisconsin Hospital & Clinics, Madison, WI, USA, in 2013. After residency, she completed a Breast Imaging Fellowship at the University of Washington, Seattle, WA, USA, in 2014. She is currently an Assistant Professor and Breast Imager with The Johns Hopkins University School of Medicine, Baltimore, MD, USA. She specializes in all aspects of breast imaging, including mammography, tomosynthesis, breast ultrasound, magnetic resonance imaging, and image-guided breast procedures. Dr. Falomo is a Board Member, certified by the American Board of Radiology.

Kelly Myers received the B.S. degree in biomedical engineering from Boston University, Boston, MA, USA, in 2003. She then attended Mount Sinai School of Medicine, New York, NY, USA, where she dedicated an additional year to research funded by a Doris Duke Fellowship Grant and received the M.D. degree in 2008. After completing diagnostic radiology residency at Johns Hopkins School of Medicine, Baltimore, MD, USA, in 2013, she performed a Breast Imaging Fellowship at the Memorial Sloan Kettering Cancer Center, New York, NY, USA. She is currently an Assistant Professor of breast imaging with the Radiology Department, Johns Hopkins University, Baltimore, MD, USA. Her research interests include the investigation of new technologies for improving the diagnosis of breast cancer.

Kelly Fabrega-Foster received the M.D. degree from the University of Medicine and Dentistry of New Jersey, Newark, NJ, USA, in 2011. After completing her internship in Internal Medicine from Crozer-Chester Medical Center, Chester, PA, USA, in 2012, she completed residency in Radiology at Johns Hopkins Hospital, Baltimore, MD, USA, in 2016. She then continued at Johns Hopkins Hospital as a Breast Imaging Fellow, where this work was completed. She is currently a Clinical Assistant Professor with the Department of Radiology, University of South Florida Morsani College of Medicine, Tampa, FL, USA.

Susan Harvey received the B.A. degree from Middlebury College, Middlebury, VT, USA, and the M.D. degree from the School of Medicine, The University of Vermont, Burlington, VT, USA. She completed an internship in internal medicine and a residency in diagnostic radiology at Yale New Haven Hospital, New Haven, CT, USA, followed by a fellowship in oncoradiology at the Brigham and Women's Hospital, Boston, MA, USA, and a fellowship in breast imaging and the treatment of breast diseases at the Dana Farber Cancer Institute, Boston, MA, USA.

Dr. Harvey is currently the Director of the Division of Breast Imaging, Johns Hopkins Radiology. Her interest in capacity building in breast cancer care for low and middle-income countries (LMICs) has also directed her work globally. She has educated radiologists in many countries as well as hosted fellowships and international advisory visits. Her goal of improving breast cancer care in LMICs is based on addressing both the resource and physician gaps in these regions. Her research interests include the efficacy of decreasing screening mammography recall rates and using abbreviated techniques for high risk screening breast magnetic resonance imaging.

Dr. Harvey is on the Board of Directors of RAD-AID, a worldwide NGO.

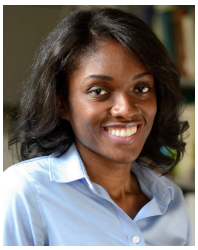

Muyinatu A. Lediju Bell (S'08–M'14) received the B.S. degree in mechanical engineering (minor in biomedical engineering) from the Massachusetts Institute of Technology, Cambridge, MA, USA, in 2006, and the Ph.D. degree in biomedical engineering from Duke University, Durham, NC, USA, in 2012. From 2009 to 2010, she conducted research abroad as a Whitaker International Fellow at The Institute of Cancer Research and Royal Marsden Hospital, Sutton, Surrey, U.K. From 2012 to 2016, she was a postdoctoral fellow with the Engineering Research Center for Computer-Integrated Surgical Systems and Technology, Johns Hopkins University, Baltimore, MD, USA.

Dr. Bell is currently an Assistant Professor in the Department Electrical and Computer Engineering with a joint appointment in the Department of Biomedical Engineering at Johns Hopkins University, where she founded and directs the Photoacoustic and Ultrasonic Systems Engineering Laboratory. Her research interests include ultrasound and photoacoustic imaging, coherence-based beamforming, image-guided surgery, robotics, and medical device design.

Dr. Bell received the NSF CAREER Award in 2018, the NIH Trailblazer Award in 2018, the MIT Technology Review's Innovator Under 35 Award in 2016, and the NIH K99/R00 Pathway to Independence Award in 2015. She currently serves as an Associate Editor of the IEEE TRANSACTIONS ON ULTRASONICS, FERROELECTRICS, AND FREQUENCY CONTROL.